# Controllable Growth of Vertical Heterostructure GaTe$_x$Se$_{1-x}$/Si by Molecular Beam Epitaxy

Shanshan Liu,[†] Xiang Yuan,[†] Peng Wang,[‡] Zhi-Gang Chen,[§] Lei Tang,[†] Enze Zhang,[†] Cheng Zhang,[†] Yanwen Liu,[†] Weiyi Wang,[†] Cong Liu,[‡] Chen Chen,[†] Jin Zou,[§] Weida Hu,*,[‡] and Faxian Xiu*,[†]

[†]State Key Laboratory of Surface Physics and Department of Physics and Collaborative Innovation Center of Advanced Microstructures, Fudan University, Shanghai 200433, China, [‡]National Laboratory for Infrared Physics, Shanghai Institute of Technical Physics, Chinese Academy of Sciences, Shanghai 200083, China, and [§]Materials Engineering, The University of Queensland, Brisbane, QLD 4072, Australia

ABSTRACT Two dimensional (2D) alloys, especially transition metal dichalcogenides, have attracted intense attention owing to their band-gap tunability and potential optoelectrical applications. Here, we report the controllable synthesis of wafer-scale, few-layer GaTe$_x$Se$_{1-x}$ alloys ($0 \leq x \leq 1$) by molecular beam epitaxy (MBE). We achieve a layer-by-layer growth mode with uniform distribution of Ga, Te, and Se elements across 2 in. wafers. Raman spectroscopy was carried out to explore the composition-dependent vibration frequency of phonons, which matches well with the modified random-element-

isodisplacement model. Highly efficient photodiode arrays were also built by depositing few-layer GaTe$_{0.64}$Se$_{0.36}$ on n-type Si substrates. These p−n junctions have steady rectification characteristics with a rectifying ratio exceeding 300 and a high external quantum efficiency around 50%. We further measured more devices on MBE-grown GaTe$_x$Se$_{1-x}$/Si heterostructures across the full range to explore the composition-dependent external quantum efficiency. Our study opens a new avenue for the controllable growth of 2D alloys with wafer-scale homogeneity, which is a prominent challenge in 2D material research.
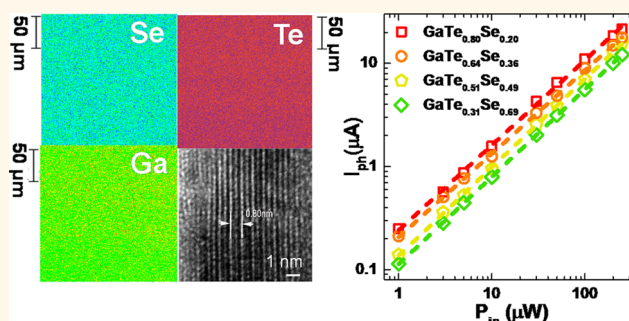
KEYWORDS: GaTe$_x$Se$_{1-x}$ · two-dimensional alloy · homogeneity · molecular beam epitaxy

The surging renewal of two-dimensional (2D) materials such as graphene,[1,2] h-BN,[3,4] black phosphorus,[5,6] transition metal dichalcogenide (TMD),[7−13] GaTe,[14] and GaSe[15−17] has attracted a great deal of attention because of their versatile and rich physical properties.[18−21] Atomically thin 2D materials have distinct electronic structure,[22,23] good carrier mobility,[24] and a layer-dependent band gap,[24] which distinguish them from their bulk crystals. The formation of heterostructures by vertically stacking 2D thin films is one crucial method to achieve full usage in optoelectronic and electronic devices.[25] Graphene/h-BN heterostructures have a novel physical property of fractional quantum Hall states.[26] With the benefit of plasmonic enhancement, solar cells based on a graphene/WSe$_2$ heterojunction achieve a maximum internal quantum efficiency up to 30%.[27] Concerning the heterostructure fabrication, molecular beam epitaxy (MBE) has outstanding merits such as easily controlled thickness of films with wafer-scale homogeneity and atomically sharp interference, which outweigh other common methods such as mechanical cleavage and transfer.[28]

While continuous efforts are devoted to the exploration of new 2D candidates, the effective alloying in 2D materials makes it possible for tunable electrical characteristics such as electron/hole density and band structure, thus enabling striking optoelectrical performance. For example, the phototransistors fabricated from MoS$_{2(1−x)}$Se$_{2x}$ alloy show a superlinear photocurrent dependence on light intensity that is distinct from mechanically cleaved MoS$_2$.[29] MoS$_{2x}$Se$_{2(1−x)}$[30−32] and Mo$_{1−x}$W$_x$S$_2$[33] alloys were experimentally proved to have bandgap tunability through controlling the sulfur and tungsten composition, respectively. Easier synthesis of ZnSn$_{1−x}$Ge$_x$N$_2$ alloy was

* Address correspondence to
(F. Xiu) faxian@fudan.edu.cn,
(W. Hu) wdhu@mail.sitp.ac.cn.

demonstrated for InGaN-based optoelectronic devices, which are difficult to grow with large-area homogeneity.[34] The band gaps of GaSe[35] and GaTe[14] are 2.0 and 1.7 eV, respectively, which are suitable energy gaps for the conversion of solar energy.[14] As for the optical devices, the photoresponsivity of GaTe phototransistors reaches 10^4 AW^{-1},[14] much higher than graphene. Combined with the direct band gap of either the thin layer or bulk crystal, GaTe has an outstanding optoelectronic performance. Also, the GaSe photodiode has a high zero-bias external quantum efficiency, fast response time, and stable photoresponse behavior, which is promising for optoelectrical measurements.[36] The latest research that focused on GaTe/Si diodes confirmed the excellent photoresponsivity with a high external quantum efficiency reaching 70%.[37] Encouraged by the appealing optoelectrical performance of GaTe and GaSe, new findings based on the alloying of these compounds are anticipated and enlightening. An elusive question is whether GaTe$_x$Se$_{1-x}$ alloys can exist and allow for a tunable photoresponsivity.

RESULTS AND DISCUSSION

In this study, we have produced wafer-scale GaTe$_x$-Se$_{1-x}$ thin films ($0 \leq x \leq 1$) by MBE. Optimal growth conditions of GaTe$_x$Se$_{1-x}$ alloys are confirmed by *in situ* reflection high-energy electron diffraction (RHEED) patterns. To identify the composition of each sample, energy-dispersive X-ray spectroscopy (EDX) has been carried out. Figure 1a displays the EDX result of the GaTe$_{0.25}$Se$_{0.75}$ alloy. Note that the asterisk (*) stands for the probed elements from the underlying mica substrate. More than 20 positions have been randomly chosen and measured, all of which show clear peaks of Ga, Se, and Te; the total error is within 4%. The inset is an optical photograph of a 2 in. transparent GaTe$_{0.25}$Se$_{0.75}$ film grown on mica. Figure S1 shows the RHEED patterns of GaTe$_x$Se$_{1-x}$ with x = 1, 0.75, 0.5, 0.25, and 0. For the pure GaTe ($x = 1$) and the pure GaSe ($x = 0$), the diffraction patterns are streaky, implying an atomically flat surface of thin films. As long as the dopants Se/Te are introduced into the system, the RHEED patterns become blurry, largely arising from the doping effect.[38] To confirm the homogeneity of the wafer-scale alloy film, the EDX mappings of Se, Te, and Ga elements in the GaTe$_{0.25}$Se$_{0.75}$ film are provided in Figure 1b. Ga, Te, and Se elements distribute uniformly over a large range of 0.16 mm × 0.16 mm. The bottom right image shows the scanning position during the measurements. To explore the structural characteristics, we carried out X-ray diffraction (XRD) and high-resolution transmission electron microscopy (HRTEM) measurements. XRD results are displayed in Figure S3, in which the distinct peaks of these alloys can be observed, which can be indexed as (003) and (006) peaks, indicating a high single crystallinity of continuous alloys with a
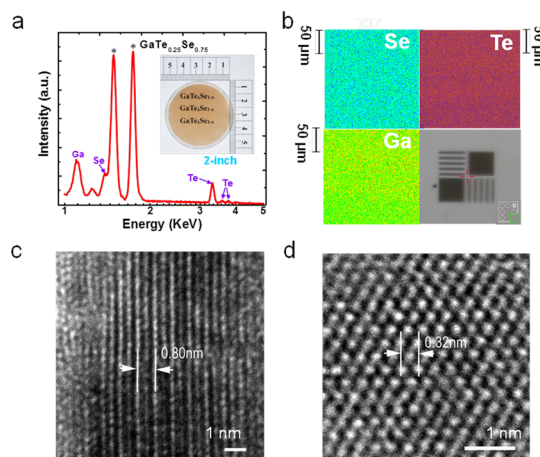
Figure 1. Characterizations of a GaTe$_{0.25}$Se$_{0.75}$ thin film. (a) EDX spectra of GaTe$_{0.25}$Se$_{0.75}$. The asterisk (*) stands for peaks originated from the mica substrate. The inset is an optical photograph of a 2 in. transparent GaTe$_{0.25}$Se$_{0.75}$ alloy grown on mica. (b) Energy dispersive X-ray spectrometer (EDX) mapping of Se, Te, and Ga in a GaTe$_{0.25}$Se$_{0.75}$ film. These elements distribute uniformly over a 0.16 mm × 0.16 mm range. The scale bar is 50 μm. The bottom right is the optical image of the scanning position. (c) HRTEM cross-section image of a GaTe$_{0.25}$Se$_{0.75}$ flake. The layer distance is 0.80 nm. The scale bar is 1 nm. (d) HRTEM image. The lattice spacing is 0.32 nm, in agreement with the (101) planes.

good composition uniformity. To be more convinced, we grew GaTe on mica and then GaSe epitaxially on the freshly grown GaTe. The measured XRD result of GaTe/GaSe is shown in Figure S3a. The peaks consist of characteristic peaks of GaSe and GaTe, totally different from those of GaTeSe alloys. For TEM characterizations, we cleaved GaTe$_{0.25}$Se$_{0.75}$ from the mica substrate and then transferred it to copper grids. Figure 1c is a typical cross-section image of the flake, where the layer distance can be measured to be 0.80 nm, which corresponds to the d spacing of (003) planes and an apparent layer separation of GaTe$_x$Se$_{1-x}$. Meanwhile, the XRD peaks in Figure S3d−f can be indexed as (003) and (006). Figure 1d is an HRTEM image of a GaTe$_{0.25}$Se$_{0.75}$ thin film at the zone axis of [0001], which validates the single-crystalline nature. A d spacing of 0.32 nm is observed, which can be assigned to (101) planes. All these results suggest that the grown GaTe$_x$-Se$_{1-x}$ alloys have a high crystallinity.

Raman spectroscopy is an important tool to explore the phonon characteristics of 2D materials.[39,40] Figure 2a shows the Raman spectra of a GaTe$_x$Se$_{1-x}$ alloy with a Te (x) composition changing from 1 to 0. Compared with the end compounds of GaTe[41] and GaSe,[42] Raman frequencies around 114 and 306 cm^{-1} are confirmed to be the A$_g$ mode.[16,41] A$_g$ stands for the out-of-plane vibration mode.[16] The Raman frequency of the A$_g$-like mode gradually shifts from 114 to 132 cm^{-1} when x decreases from 1 to 0. Also, the A$_{1g}^2$ peaks have a blue shift as well, similar to the evolution of the A$_g$-like mode. It reaches a maximum of 306 cm^{-1} at $x = 0$, a characteristic Raman peak of GaSe.[42] The peak at
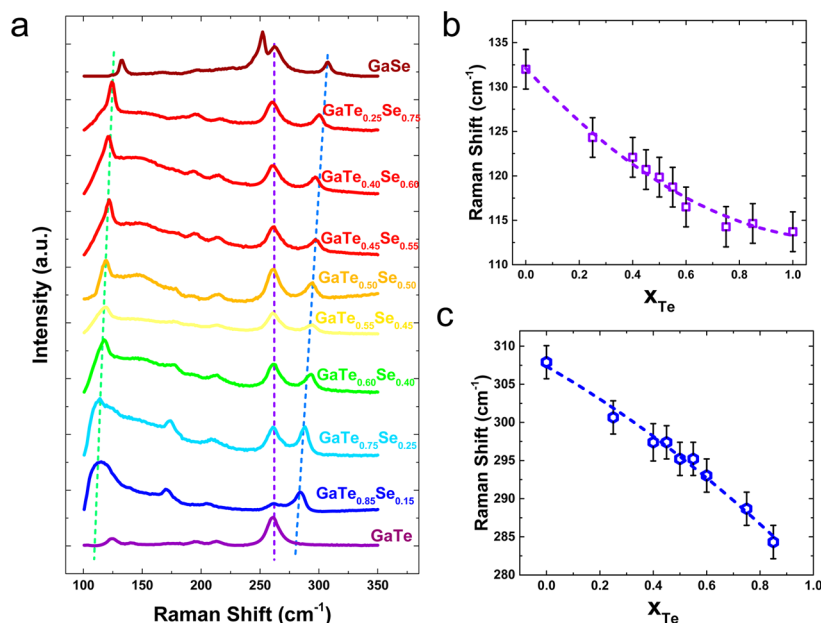
Figure 2. Raman spectra of GaTe$_x$Se$_{1-x}$ alloys. (a) Composition-dependent Raman spectra of GaTe$_x$Se$_{1-x}$ alloys with x from 1 to 0 in the range 100 and 350 cm^{-1}. The Raman A$_g$-like peak has a blue-shift from 114 to 132 cm^{-1} with x from 1 to 0. The A$_{1g}^2$ peak has a blue-shift as well and reaches a maximum of 306 cm^{-1} at $x = 0$. The peak at 250 cm^{-1} is from the mica substrate. (b) Raman frequency of the A$_g$-like peak as a function of Te composition. The rectangles are the experimental data, and the dashed line is the theoretical simulations based on the MREI model. The experimental data match well with the theory. (c) Composition-dependent Raman frequency of the A$_{1g}^2$ peak.

250 cm^{-1} originates from the mica substrate. Figure 2b is the Raman frequency of the A$_g$-like peak as a function of Te composition. With increasing Te concentration, the frequency of the A$_g$-like mode decreases monotonically, and the purple rectangles represent the experimental data.

The modified random-element-isodisplacement (MREI) model has effectively explained the Raman shifts of mixed crystals, such as AB$_x$C$_{1-x}$ type and AB$_x$C$_{2-x}$ type.[39,43] The MREI model is based on the random distribution of substituted atoms and isodisplacement, like the same atoms vibrating in the same amplitude and phase.[39] On the basis of the EDX data, random distributions of Te and Se are confirmed throughout the sample, and therefore the MREI model is effective to elucidate the Raman changes in our scenario. On the basis of the calculation of the MREI model, the displacements of Ga, Te, and Se atoms can be written as follows:[44]

Ga: $m_g x x_g = -x F_t (X_g - X_t) - (1 - X) F_s (X_g - X_s)$

Te: $m_t x x_t = -F_t (X_t - X_g) - (1 - X) F_i (X_t - X_s)$

Se: $m_t x x_s = -F_s (X_s - X_g) - x F_i (X_s - X_t)$

where X_g, X_t, and X_s are the displacements of the atoms Ga, Te, and Se and x_g, x_t, and x_s are the second derivative of the respective displacements; m_g, m_t, and m_s are the masses of Ga, Te, and Se atoms, respectively; F_s, F_t, and F_i are the interaction force constants of Ga–Se, Ga–Te, and Se–Te. The function of the force constant is assumed to vary linearly with

composition x; that is, $F_t/F_{t0} = F_s/F_{s0} = F_{t0} = F_i/F_{i0} = 1 - \theta x$, where F_{s0}, F_{t0}, and F_{i0} are the limiting values of the force constant as $x \rightarrow 0$ and θ can be determined from the thermal expansion, compressibility, etc. Through a sequence of operations, the Raman frequency ω of the A$_g$ mode can be written as

$$\omega^2 = 0.5(1 - \theta x)\left[F_{s0}\left(\frac{1-x}{m_{Ga}} + \frac{1}{m_{Se}}\right) + F_{t0}\left(\frac{x}{m_{Ga}} + \frac{1}{m_{Te}}\right) \right.$$

$$+ F_{i0}\left(\frac{1-x}{m_{Te}} + \frac{x}{m_{Se}}\right) \pm \left(\left(F_{s0}\left(\frac{1-x}{m_{Ga}} + \frac{1}{m_{Se}}\right)\right.\right.$$

$$+ F_{t0}\left(\frac{x}{m_{Ga}} + \frac{1}{m_{Te}}\right) + F_{i0}\left(\frac{1-x}{m_{Ga}} + \frac{1}{m_{Se}}\right)\right)^2$$

$$\left.\left. + 4x(1-x)\left(\frac{F_{t0}}{m_{Ga}} - \frac{F_{t0}}{m_{Se}}\right)\left(\frac{F_{s0}}{m_{Ga}} - \frac{F_{i0}}{m_{Te}}\right)\right)^{1/2}\right]$$

The values of ω for different Te composition (x) can be calculated from this formula. Given the boundary condition of $x = 1, 0$ and Gruneisen's relation,[45] F_{s0}, F_{t0}, and F_{i0}, and θ are calculated to be 1.52 × 10^6, 2.21 × 10^5, and 6.85 × 10^5 amu cm^{-2} and −0.071, respectively. After substituting these parameters into the equation the simulation data are displayed as the dashed line in Figure 2b, where the data match well with the theoretical calculations. Figure 2c is the composition-dependent Raman frequency of the A$_{1g}^2$ peak. Similarly, the dashed line represents the theoretical simulation results based on the MREI model. Therefore, the development of the A$_g$ mode
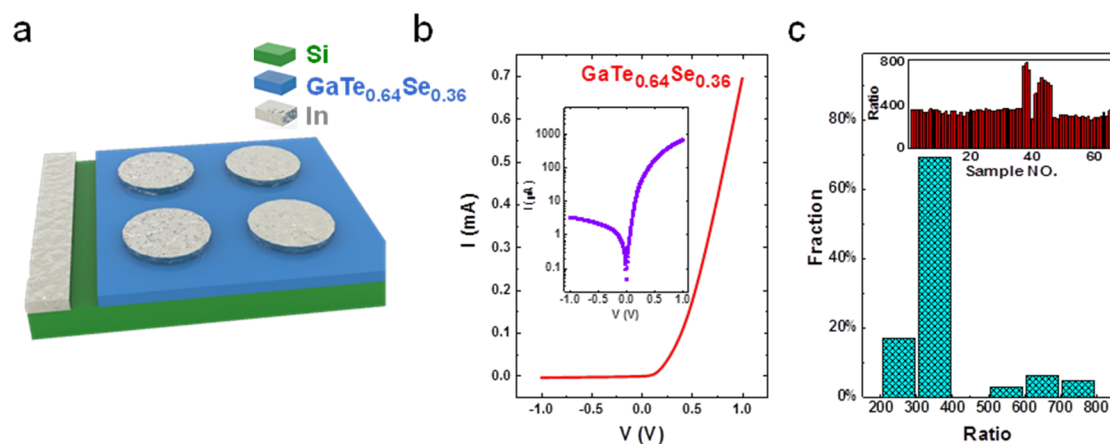
Figure 3. $I-V$ characteristics of a $GaTe_{0.64}Se_{0.36}$/Si p−n diode. (a) Schematic geometry of the p−n diode. From the top to the bottom, layers are In as the anode, p-$GaTe_xSe_{1-x}$, n-Si; the left bottom contact is In, as the cathode. (b) $I-V$ curve. The rectifying ratio is larger than 300. The inset is a logarithm plot of the $I-V$ curve with absolute values, showing a clear rectifying characteristic. (c) Rectifying ratio distribution of randomly selected diodes. The rectifying ratio is centered at 300−400, exactly 70% of the chosen diodes. The inset is the performance of each p−n diode.

in our Raman spectra can be used to distinguish the composition of alloys.

To explore the optoelectrical properties of the $GaTe_x$-Se_{1-x} alloys, we have deposited 8 nm $GaTe_xSe_{1-x}$ thin films on Si to form vertical p−n junctions, and unless specially mentioned the thickness of $GaTe_xSe_{1-x}$ is the same hereafter. To remove the oxidation and organic residues, Si substrates were cleaned by RCA process,[46] immediately were loaded into an ultra-high-vacuum (UHV) chamber, and then annealed at 850 °C for 30 min. Figure 3a is the schematic diagram of $GaTe_x$-Se_{1-x}/Si heterojunctions. From the top to the bottom, the structure consists of In, $GaTe_xSe_{1-x}$, and Si. Figure 3b reveals a current−voltage ($I-V$) curve of the $GaTe_{0.64}Se_{0.36}$/Si diode, showing a typical rectification characteristic. The rectifying ratio of $GaTe_{0.64}$-$Se_{0.36}$/Si, defined as the ratio of current biased by +1 V and −1 V, exceeds 300. The inset is the absolute current value as a function of the biased voltage. The distribution of the rectification characteristic is shown in Figure 3c. Among the 65 randomly selected p−n diodes across the 3 in. Si wafer, the rectifying ratio lies between 300 and 400 (70% of diodes), which can be positive evidence for the wafer-scale homogeneity.

To enhance the transmittance of laser incident energy on the diodes, transparent indium tin oxide (ITO) is used for constructing the anode. The experimental setup for photocurrent measurements is shown in Figure 4a. The structure of the diode is the same as that displayed in Figure 3a except that the top layer is replaced with ITO for optimized light transmittance. Figure 4b shows the biased voltage-dependent current under different incident power levels. With the incident power increasing, the photocurrent rises due to the generation of more electron−hole pairs. Under a certain laser incident power, however, the photocurrent increases initially with the negative bias-voltage and then reaches a saturation. This can be attributed to

the fact that an increased bias-voltage can separate electron−hole pairs more efficiently, then leading to a larger photocurrent, whereas it gradually saturates as the voltage goes beyond a certain value due to the limited number of carriers generated by the fixed incident power.[47] Figure 4c is the histogram of the zero-biased photocurrent distribution under a laser incident power of 250 μW, which shows that the photocurrent of 90% of the photodiodes is larger than 12 μA among all the randomly selected diodes. Figure 4d displays the zero-biased photocurrent under different laser incident powers. Within the laser power range of 1 to 250 μW, the photocurrent increases with the higher power. On the logarithmic scale the photocurrent and the incident power follow a linear behavior. Photoresponsivity is defined as the generated photocurrent per incident laser power. It can be described by the equation R = I_{ph}/P_{in}, where I_{ph} is defined as $I_{ph} = I_{light} - I_{dark}$. Zero-biased photoresponsivity under 1 μW incident light power is calculated to be 0.21 AW^{-1}. The inset of Figure 4d is the zero-biased photocurrent mapping at a corner of a $GaTe_{0.64}$-$Se_{0.36}$/Si photodiode under the laser power of 250 μW. The photocurrent distributes uniformly within the junction of $GaTe_{0.64}Se_{0.36}$ and Si and decreases to nearly zero as the laser beam moves far away from the junction area. Therefore, we can verify the formation of a vertical $GaTe_{0.64}Se_{0.36}$/Si heterostructure instead of the lateral p−n junction.[48] Another criterion of photodetectors, external quantum efficiency (EQE), similar to photoresponsivity, is defined as the number of photogenerated carriers per incident photon, calculated by EQE = $I_{ph}/q\phi = (I_{ph}/q)(h\nu/P_{in})$, where I_{ph} is photocurrent, q is electron charge, h is Planck's constant, and ν and P_{in} are the frequency and power of the incident laser, respectively. Zero-biased EQE of the $GaTe_{0.64}Se_{0.36}$/Si photodiode is displayed in Figure 4e. As the incident power decreases, the EQE increases and

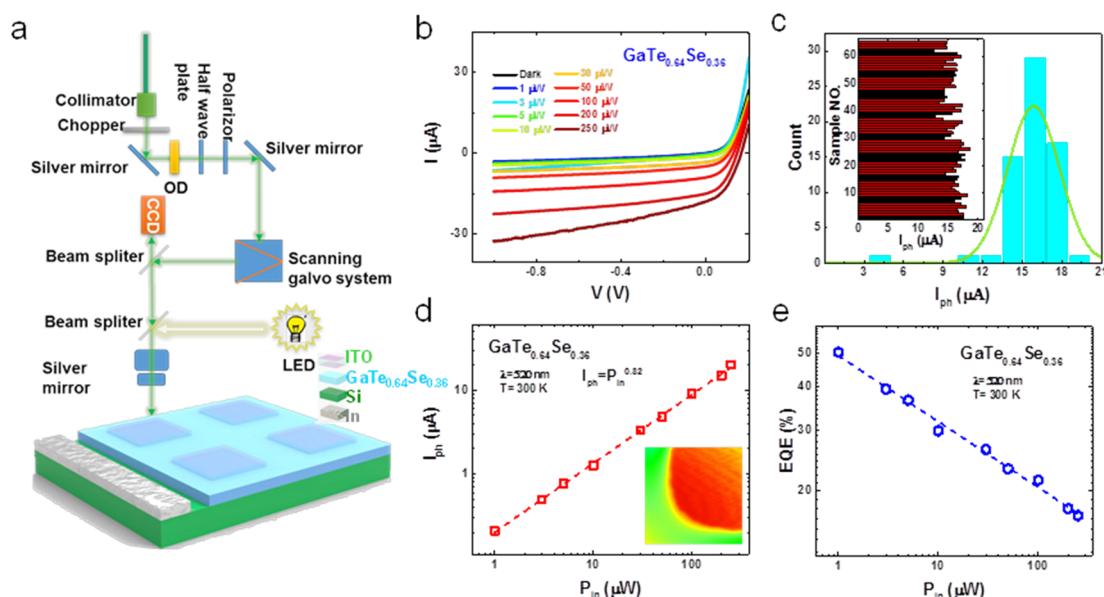**Figure 4.** Photoresponse characteristics of a $GaTe_{0.64}Se_{0.36}$/Si photodiode. (a) Sketch of the photoelectric experimental setup. (b) Photocurrent as a function of biased voltage under different laser power. (c) Photocurrent distribution of randomly selected diodes. The incident laser power is 250 μW. The photocurrent of 90% of the diodes is focused between 12.5 and 18 μA; the inset is the performance of each photodiode. (d) Zero-biased photocurrent as a function of incident power. The inset is a photocurrent mapping of a p−n junction corner. (e) Zero-biased external quantum efficiency. The horizontal axis denotes the incident power.
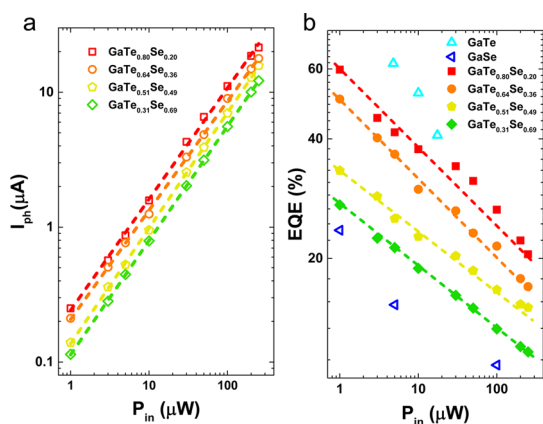

Figure 5. Composition dependent (a) photocurrent and (b) EQE under different laser intensities. As the laser power increases, the photocurrent rises exponentially, while the EQE declines exponentially. As the Te composition decreases, the photocurrent and EQE drop.

reaches a maximum of 50% under 1 μW (the ideal value is 100%),[49] showing a competitive advantage over the previously reported p−n photodiodes.[50,51]

Different compositions of $GaTe_xSe_{1-x}$ alloys may induce diverse behavior. We have varied the Te composition and produced three additional photodiodes of $GaTe_{0.31}Se_{0.69}$/Si, $GaTe_{0.51}Se_{0.49}$/Si, and $GaTe_{0.80}Se_{0.20}$/Si. Their zero-biased photocurrents and EQE are presented

in Figure 5a and b, respectively. With decreasing laser power, the EQE rises linearly, similar to that shown in Figure 4e. Under a certain incident power, samples containing more Te have a larger photocurrent and EQE; that is, with increasing Te composition the photocurrent and EQE have a rising trend. Consequently, the composition-dependent EQE variation is a rational result in view of previous findings on GaTe and GaSe that the EQE of GaTe photodiodes is larger than that of the GaSe photodetectors.[36,37]

CONCLUSIONS

In conclusion, wafer-scale $GaTe_xSe_{1-x}$ films are successfully grown by MBE, and high crystallinity is confirmed by XRD and HRTEM measurements. On the basis of the MREI model, the Raman spectra can be used to distinguish the composition of the alloys. The arrayed vertical p−n heterojunction $GaTe_{0.64}Se_{0.36}$/Si shows an excellent rectifying characteristic. Photodetectors based on $GaTe_{0.64}Se_{0.36}$/Si photodiodes have a large external quantum efficiency. With increasing Te composition, the photocurrent and EQE have a consistent variation that the more Te is doped into GaSe, the higher photocurrent and EQE the device will yield. Combined with the state-of-the-art silicon technology, our 2D heterojunction is promising for practical electronic and optoelectronic applications.

METHODS

Thin-Film Synthesis. Layered $GaTe_xSe_{1-x}$ was grown on freshly cleaved mica or cleaned silicon substrates in a PerkinElmer

430 MBE system. Silicon substrates were cleaned by following the commonly used and well-established RCA (Radio Corporation of America) process and then annealed at 850 °C under ultra-high-vacuum conditions for 30 min. High-purity Ga, Te,

and Se fluxes are evaporated from Standard Knudsen cells through heating. The flux of each cell is measured by a crystal oscillator. The growth temperature was set to be 600 °C.

Thin-Film Characterizations. Raman spectroscopy measurements were performed with a Renishaw-inVia confocal Raman system with a laser wavelength of 632.8 nm. The diameter of the focused laser spot is 3 μm. Energy-dispersive X-ray spectrometer measurements were taken with an EPMA-1720/1720H system. Structure characterizations of $GaTe_xSe_{1-x}$ thin films were explored by XRD (Bruker D8 Discover) and HRTEM (FEI Tecnai F20).

Electrical and Optoelectrical Characterizations. Electrical characteristics and photoresponse measurements were carried out by using an Agilent 2902. The incident light from a 520 nm laser is initially focused and then illuminated on the samples. Laser intensity was controlled by a series of neutral density filters and a linear polarizer/wave-plate. The calibration of laser power was accomplished with a Thorlab-S130C photodiode power sensor. To do the spatially resolved photocurrent measurements, a galvanometer, operated by an open-source controller, was used for controlling the laser spot scanning across the device.

Conflict of Interest: The authors declare no competing financial interest.

Supporting Information Available: The Supporting Information is available free of charge on the ACS Publications website at DOI: 10.1021/acsnano.5b03796.

Extra structural characterizations of $GaTe_xSe_{1-x}$ and optoelectrical performance of $GaTe_xSe_{1-x}$/Si photodiodes (PDF)

REFERENCES AND NOTES

1. Kim, K. S.; Zhao, Y.; Jang, H.; Lee, S. Y.; Kim, J. M.; Kim, K. S.; Ahn, J. H.; Kim, P.; Choi, J. Y.; Hong, B. H. Large-Scale Pattern Growth of Graphene Films for Stretchable Transparent Electrodes. *Nature* **2009**, *457*, 706–710.
2. Zhang, Y.; Tan, Y. W.; Stormer, H. L.; Kim, P. Experimental Observation of The Quantum Hall Effect and Berry's Phase in Graphene. *Nature* **2005**, *438*, 201–204.
3. Zhi, C.; Bando, Y.; Tang, C.; Kuwahara, H.; Golberg, D. Large-Scale Fabrication of Boron Nitride Nanosheets and Their Utilization in Polymeric Composites with Improved Thermal and Mechanical Properties. *Adv. Mater.* **2009**, *21*, 2889–2893.
4. Lee, K. H.; Shin, H. J.; Lee, J.; Lee, I. Y.; Kim, G. H.; Choi, J. Y.; Kim, S. W. Large-Scale Synthesis of High-Quality Hexagonal Boron Nitride Nanosheets for Large-Area Graphene Electronics. *Nano Lett.* **2012**, *12*, 714–718.
5. Li, L.; Yu, Y.; Ye, G. J.; Ge, Q.; Ou, X.; Wu, H.; Feng, D.; Chen, X. H.; Zhang, Y. Black Phosphorus Field-Effect Transistors. *Nat. Nanotechnol.* **2014**, *9*, 372–377.
6. Dolui, K.; Quek, S. Y. Quantum-Confinement and Structural Anisotropy Result in Electrically-Tunable Dirac Cone in Few-layer Black Phosphorous. *arXiv:1503.03647*, **2015**.
7. Keum, D. H.; Cho, S.; Kim, J. H.; Choe, D.-H.; Sung, H.-J.; Kan, M.; Kang, H.; Hwang, J.-Y.; Kim, S. W.; Yang, H. Bandgap Opening in Few-Layered Monoclinic $MoTe_2$. *Nat. Phys.* **2015**, *11*, 482–486.
8. Srivastava, A.; Sidler, M.; Allain, A. V.; Lembke, D. S.; Kis, A.; Imamoğlu, A. Valley Zeeman Effect in Elementary Optical Excitations of Monolayer WSe_2. *Nat. Phys.* **2015**, *11*, 3203.
9. Yuan, H.; Wang, X.; Lian, B.; Zhang, H.; Fang, X.; Shen, B.; Xu, G.; Xu, Y.; Zhang, S. C.; Hwang, H. Y.; et al. Generation and Electric Control of Spin-Valley-Coupled Circular Photogalvanic Current in WSe_2. *Nat. Nanotechnol.* **2014**, *9*, 851–857.
10. Ali, M. N.; Xiong, J.; Flynn, S.; Tao, J.; Gibson, Q. D.; Schoop, L. M.; Liang, T.; Haldolaarachchige, N.; Hirschberger, M.; Ong, N. P.; et al. Large, Non-Saturating Magnetoresistance in WTe_2. *Nature* **2014**, *514*, 205–208.
11. Kang, K.; Xie, S.; Huang, L.; Han, Y.; Huang, P. Y.; Mak, K. F.; Kim, C.-J.; Muller, D.; Park, J. High-Mobility Three-Atom-Thick Semiconducting Films With Wafer-Scale Homogeneity. *Nature* **2015**, *520*, 656–660.
12. Nan, H.; Wang, Z.; Wang, W.; Liang, Z.; Lu, Y.; Chen, Q.; He, D.; Tan, P.; Miao, F.; Wang, X. Strong Photoluminescence Enhancement of MoS_2 through Defect Engineering and Oxygen Bonding. *ACS Nano* **2014**, *8*, 5738–5745.
13. Zhang, Y.; Chang, T. R.; Zhou, B.; Cui, Y. T.; Yan, H.; Liu, Z.; Schmitt, F.; Lee, J.; Moore, R.; Chen, Y.; et al. Direct Observation of the Transition from Indirect to Direct Bandgap in Atomically Thin Epitaxial $MoSe_2$. *Nat. Nanotechnol.* **2014**, *9*, 111–115.
14. Wang, Z.; Safdar, M.; Mirza, M.; Xu, K.; Wang, Q.; Huang, Y.; Wang, F.; Zhan, X.; He, J. High-Performance Flexible Photodetectors Based on GaTe Nanosheets. *Nanoscale* **2015**, *7*, 7252–7258.
15. Jian, S.-R.; Juang, J.-Y.; Luo, C.-W.; Ku, S.-A.; Wu, K.-H. Nanomechanical Properties of GaSe Thin Films Deposited on Si(111) Substrates by Pulsed Laser Deposition. *J. Alloys Compd.* **2012**, *542*, 124–127.
16. Lei, S.; Ge, L.; Liu, Z.; Najmaei, S.; Shi, G.; You, G.; Lou, J.; Vajtai, R.; Ajayan, P. M. Synthesis and Photoresponse of Large GaSe Atomic Layers. *Nano Lett.* **2013**, *13*, 2777–2781.
17. Hu, P.; Wen, Z.; Wang, L.; Tan, P.; Xiao, K. Synthesis of Few-Layer GaSe Nanosheets for High Performance Photodetectors. *ACS Nano* **2012**, *6*, 5988–5994.
18. Yin, Z.; Li, H.; Li, H.; Jiang, L.; Shi, Y.; Sun, Y.; Lu, G.; Zhang, Q.; Chen, X.; Zhang, H. Single-Layer MoS_2 Phototransistors. *ACS Nano* **2012**, *6*, 74–80.
19. Lopez-Sanchez, O.; Lembke, D.; Kayci, M.; Radenovic, A.; Kis, A. Ultra-Sensitive Photodetectors Based on Monolayer MoS_2. *Nat. Nanotechnol.* **2013**, *8*, 497–501.
20. Baugher, B. W.; Churchill, H. O.; Yang, Y.; Jarillo-Herrero, P. Optoelectronic Devices Based on Electrically Tunable p-n Diodes in a Monolayer Dichalcogenide. *Nat. Nanotechnol.* **2014**, *9*, 262–267.
21. Pospischil, A.; Furchi, M. M.; Mueller, T. Solar-Energy Conversion and Light Emission in an Atomic Monolayer $p-n$ Diode. *Nat. Nanotechnol.* **2014**, *9*, 257–261.
22. Neto, A. C.; Guinea, F.; Peres, N.; Novoselov, K. S.; Geim, A. K. The Electronic Properties of Graphene. *Rev. Mod. Phys.* **2009**, *81*, 109–162.
23. Xu, X.; Yao, W.; Xiao, D.; Heinz, T. F. Spin and Pseudospins in Layered Transition Metal Dichalcogenides. *Nat. Phys.* **2014**, *10*, 343–350.
24. Wang, Q. H.; Kalantar-Zadeh, K.; Kis, A.; Coleman, J. N.; Strano, M. S. Electronics and Optoelectronics of Two-Dimensional Transition Metal Dichalcogenides. *Nat. Nanotechnol.* **2012**, *7*, 699–712.
25. Hong, X.; Kim, J.; Shi, S. F.; Zhang, Y.; Jin, C.; Sun, Y.; Tongay, S.; Wu, J.; Zhang, Y.; Wang, F. Ultrafast Charge Transfer in Atomically Thin MoS(2)/WS(2) Heterostructures. *Nat. Nanotechnol.* **2014**, *9*, 682–686.
26. Zhang, C.; Zhao, S.; Jin, C.; Koh, A. L.; Zhou, Y.; Xu, W.; Li, Q.; Xiong, Q.; Peng, H.; Liu, Z. Direct Growth of Large-Area Graphene and Boron Nitride Heterostructures by a co-Segregation Method. *Nat. Commun.* **2015**, *6*, 6519.
27. Zhang, M.; Wu, J.; Zhu, Y.; Dumcenco, D. O.; Hong, J.; Mao, N.; Deng, S.; Chen, Y.; Yang, Y.; Jin, C. Two-Dimensional Molybdenum Tungsten Diselenide Alloys: Photoluminescence, Raman Scattering, and Electrical Transport. *ACS Nano* **2014**, *8*, 7130–7137.
28. Song, X.; Hu, J.; Zeng, H. Two-Dimensional Semiconductors: Recent Progress and Future Perspectives. *J. Mater. Chem. C* **2013**, *1*, 2952–2969.
29. Klee, V.; Preciado, E.; Barroso, D.; Nguyen, A. E.; Lee, C.; Erickson, K. J.; Triplett, M.; Davis, B.; Lu, I.-H.; Bobek, S. Superlinear Composition-Dependent Photocurrent in CVD-Grown Monolayer MoS_2 (1−x) Se2 x Alloy Devices. *Nano Lett.* **2015**, *15*, 2612–2619.
30. Li, H.; Duan, X.; Wu, X.; Zhuang, X.; Zhou, H.; Zhang, Q.; Zhu, X.; Hu, W.; Ren, P.; Guo, P.; et al. Growth of Alloy

MoS(2x)Se2(1-x) Nanosheets with Fully Tunable Chemical Compositions and Optical Properties. *J. Am. Chem. Soc.* **2014**, *136*, 3756–3759.

31. Li, H.; Zhang, Q.; Duan, X.; Wu, X.; Fan, X.; Zhu, X.; Zhuang, X.; Hu, W.; Zhou, H.; Pan, A.; et al. Lateral Growth of Composition Graded Atomic Layer MoS2(1-x)Se2x Nanosheets. *J. Am. Chem. Soc.* **2015**, *137*, 5284–5287.

32. Mann, J.; Ma, Q.; Odenthal, P. M.; Isarraraz, M.; Le, D.; Preciado, E.; Barroso, D.; Yamaguchi, K.; von Son Palacio, G.; Nguyen, A.; et al. 2-Dimensional Transition Metal Dichalcogenides with Tunable Direct Band Gaps: MoS(2)((1)-x) Se(2)x Monolayers. *Adv. Mater.* **2014**, *26*, 1399–1404.

33. Chen, Y.; Xi, J.; Dumcenco, D. O.; Liu, Z.; Suenaga, K.; Wang, D.; Shuai, Z.; Huang, Y.-S.; Xie, L. Tunable Band Gap Photoluminescence from Atomically Thin Transition-Metal Dichalcogenide Alloys. *ACS Nano* **2013**, *7*, 4610–4616.

34. Narang, P.; Chen, S.; Coronel, N. C.; Gul, S.; Yano, J.; Wang, L. W.; Lewis, N. S.; Atwater, H. A. Bandgap Tunability in Zn(Sn,Ge)N(2) Semiconductor Alloys. *Adv. Mater.* **2014**, *26*, 1235–1241.

35. Li, X.; Lin, M. W.; Puretzky, A. A.; Idrobo, J. C.; Ma, C.; Chi, M.; Yoon, M.; Rouleau, C. M.; Kravchenko, I. I.; Geohegan, D. B.; et al. Controlled Vapor Phase Growth of Single Crystalline, Two-Dimensional GaSe Crystals with High Photoresponse. *Sci. Rep.* **2014**, *4*, 5497.

36. Yuan, X.; Tang, L.; Liu, S.; Wang, P.; Chen, Z.; Zhang, C.; Liu, Y.; Wang, W.; Zou, Y.; Liu, C.; et al. Arrayed Van der Waals Vertical Heterostructures Based on 2D GaSe Grown by Molecular Beam Epitaxy. *Nano Lett.* **2015**, *15*, 3571–3577.

37. Yuan, X.; Tang, L.; Wang, P.; Chen, Z.; Zou, Y.; Su, X.; Zhang, C.; Liu, Y.; Wang, W.; Liu, C.; et al. Wafer-Scale Arrayed *p-n* Junctions Based on Few-Layer Epitaxial GaTe. *arXiv:1412.4884*, **2014**.

38. Fujita, S.; Nakaoka, Y.; Uemura, T.; Tabuchi, M.; Noda, S.; Takeda, Y.; Sasaki, A. Rheed and X-Ray Characterization of InGaAs/GaAs Grown by MBE. *J. Cryst. Growth* **1989**, *95*, 224–227.

39. Chen, Y.; Dumcenco, D. O.; Zhu, Y.; Zhang, X.; Mao, N.; Feng, Q.; Zhang, M.; Zhang, J.; Tan, P. H.; Huang, Y. S.; et al. Composition-Dependent Raman Modes of Mo(1-x)W(x)S2 Monolayer Alloys. *Nanoscale* **2014**, *6*, 2833–2839.

40. Lu, W.; Nan, H.; Hong, J.; Chen, Y.; Zhu, C.; Liang, Z.; Ma, X.; Ni, Z.; Jin, C.; Zhang, Z. Plasma-Assisted Fabrication of Monolayer Phosphorene and its Raman Characterization. *Nano Res.* **2014**, *7*, 853–859.

41. Liu, F.; Shimotani, H.; Shang, H.; Kanagasekaran, T.; Zolyomi, V.; Drummond, N.; Fal'ko, V. I.; Tanigaki, K. High-Sensitivity Photodetectors Based on Multilayer GaTe Flakes. *ACS Nano* **2014**, *8*, 752–760.

42. Zhou, Y.; Nie, Y.; Liu, Y.; Yan, K.; Hong, J.; Jin, C.; Zhou, Y.; Yin, J.; Liu, Z.; Peng, H. Epitaxy and Photoresponse of Two-Dimensional GaSe Crystals on Flexible Transparent Mica Sheets. *ACS Nano* **2014**, *8*, 1485–1490.

43. Chanchal; Garg, A. K. MREI-Model Calculations of Optical Phonons in Layered Mixed Crystals of 2H-Polytype of The Series SnS2−xSex (0 ≤ x ≤ 2). *Phys. B* **2006**, *383*, 188–193.

44. Chen, Y. S.; Shockley, W.; Pearson, G. L. Lattice Vibration Spectra of GaAsxP1−x Single Crystals. *Phys. Rev.* **1966**, *151*, 648–656.

45. Kittel, C.; Holcomb, D. F. Introduction to Solid State Physics. *Am. J. Phys.* **1967**, *35*, 547–548.

46. Kern, W. *Handbook of Semiconductor Wafer Cleaning Technology*; Noyes Publication: NJ, 1993; pp 111−196.

47. Koster, L. J. A.; Mihailetchi, V. D.; Ramaker, R.; Blom, P. W. Light Intensity Dependence of Open-Circuit Voltage of Polymer: Fullerene Solar Cells. *Appl. Phys. Lett.* **2005**, *86*, 123509–123512.

48. Sze, S. M. *Semiconductor Devices: Physics and Technology*; John Wiley & Sons: New York, 2008.

49. Sun, Z.; Chang, H. Graphene and Graphene-like Two-Dimensional Materials in Photodetection: Mechanisms and Methodology. *ACS Nano* **2014**, *8*, 4133–4156.

50. Koppens, F. H.; Mueller, T.; Avouris, P.; Ferrari, A. C.; Vitiello, M. S.; Polini, M. Photodetectors Based on Graphene, other Two-Dimensional Materials and Hybrid Systems. *Nat. Nanotechnol.* **2014**, *9*, 780–793.

51. Konstantatos, G.; Sargent, E. H. Nanostructured Materials for Photon Detection. *Nat. Nanotechnol.* **2010**, *5*, 391–400.